Supporting Information for

Revealing Energetics of Surface Oxygen Redox from Kinetic Fingerprint in Oxygen Electrocatalysis

Hua Bing Tao,[a] Junming Zhang,[a] Jiazang Chen,[c] Liping Zhang,[a] Yinghua Xu,[d]

Jingguang G. Chen,[b,*] and Bin Liu[a,*]

[a]School of Chemical and Biomedical Engineering, Nanyang Technological University, 62 Nanyang Drive, Singapore 637459, Singapore

[b]Department of Chemical Engineering, Columbia University, New York, NY 10027, United States

[c]State Key Laboratory of Coal Conversion, Institute of Coal Chemistry, Chinese Academy of Sciences, Taiyuan 030001, China

[d]State Key Laboratory Breeding Base of Green Chemistry-Synthesis Technology, College of Chemical Engineering, Zhejiang University of Technology, Hangzhou 310032, China

[*]To whom correspondence should be addressed. Email: jgchen@columbia.edu (J.G. Chen) liubin@ntu.edu.sg (B. Liu)

Table of contents

1 Experimental section

1.1 Catalyst synthesis and working electrode preparation

The synthesis methods for Fe_2O_3, Co_3O_4, TiO_2 and α-MnO_2 nanostructured catalysts are the same as those used in our previous work.[1] RuO_2 nanoparticles were prepared according to a reported method.[2] Surface density of coordinatively unsaturated metal (M_{CUS}) on transition metal oxides such as α-MnO_2 was tuned by the method developed in our previous work.[1] The (oxy)hydroxides of Ni, Co, Fe, Mn are prepared through electrodeposition method. Specifically, 0.1 M MCl_2 (M refers to Ni, Co, Fe, Mn) solution is used as precursor for electrodeposition. Pre-cleaned glassy carbon rotating disk electrode (RDE) or rotating ring-disk electrode (RRDE) is used as substrate for electrodeposition by galvanostatic mode with a cathodic current density of 0.5 mA cm^{-2} lasting 100s. NiFe and CoFe are electrodeposited under same conditions in mixed solution of the metal salt (the optimized NiFe and CoFe are obtained with 50% and 20% Fe respectively). The electrodeposited thin films are rinsed with high purity water prior to electrochemical tests.

Materials characterization and temperature programmed reduction (TPR) were performed with the same procedure as described before. To prepare a working electrode, the catalysts were first dispersed in an isopropyl alcohol (IPA)/water (v : v = 1 : 1) solution or pure N,N-dimethylformamide (99.8%, Sigma-Aldrich) with a concentration of 2 mg/ml. Since α-MnO_2 is difficult to be well dispersed in solution, we mixed α-MnO_2 catalyst with multi-walled carbon nanotubes (MWCNTs) with a weight ratio α-MnO_2 : MWCNTs = 4 : 1 to get a well-dispersed ink. The mixture was sonicated for 1 h, and subsequently, certain amount of the catalyst solution was drop-casted onto a pre-cleaned glassy carbon (GC) rotating disk electrode (0.196 cm^2, Pine Instruments). The electrode was dried in atmosphere overnight before

electrochemical test. Catalyst loading for OER tests is 100 μg/cm^2, while the loading is 500 μg/cm^2 for non-Pt catalysts and 100 μg/cm^2 for Pt/C in ORR. The same loading was used in rotating ring-disk electrode (RRDE), where the disk is 0.282 cm^2 glassy carbon and the ring is 0.126 cm^2 Pt (Pine Instruments). For kinetic comparison of optimized α-MnO_2 catalyst with Pt/C, carbon fibre paper was used as the substrate with effective area of 0.5 cm^2. α-MnO_2 H-250 and Pt/C were deposited on one side of carbon fibre paper with loading of 600 μg/cm^2 and 200 μg/cm^2, respectively.

1.2 Electrochemical studies

Electrochemical tests were conducted on an Autolab PGSTAT 30 with a three-electrode configuration. Specially designed **glass-free cell** (provided by Hangzhou Saiao Electrochemical Technology Co., LTD) was used in all electrochemical tests to eliminate the influence of glass components on the activity of catalysts.[3] Pt plate (1 cm^2) was used as the counter electrode only in the OER tests. Considering the significant dissolution of Pt at high positive potential,[4] large area titanium plate (~ 8 cm^2) was selected as the counter electrode in ORR tests or for reference electrode calibration to avoid the contamination of electrolyte and working electrodes. Saturated calomel electrode (SCE) was used as the reference electrode and was calibrated with home-made reversible hydrogen electrode (RHE). Specifically, a pre-cleaned Pt wire was used as the working electrode with Ti plate and SCE as counter and reference electrode, respectively. The electrolyte is the same as that used in the following electrochemical tests. After saturation of the electrolyte with ultrahigh purity H_2 (99.9995%, from Air Liquid Singapore), 6 cyclic voltammetry (CV) scans at a low scan rate (1 mV/s) was carried out in the potential range of hydrogen evolution/oxidation (typically from -1.2 V to -0.8 V vs SCE). Once the CVs become stable, the potential under which the current switches from positive to negative, or vice versa, is the RHE. To reduce the effects of impurities, **high**

purity KOH (semiconductor grade, 99.99% trace metals basis, Siama-Aldrich) was used throughout the electrochemical tests. The potential of SCE in 1 M KOH electrolyte was calibrated to be 1.049 V vs RHE, consistent with 1.051 V vs RHE from the literature.[5]

The electrochemical tests were conducted at a rotating speed of 1600 rpm in 1 M KOH electrolyte (pH = 13.72) to minimize mass transport limit. For RRDE tests, the potential of ring working electrode was held at 1.15 V vs RHE, under which the current collection efficiency is 0.24.[6] All polarization curves were corrected by eliminating the *iR* drop in the electrical circuit. Relatively low scan rate (1 mV/s) was employed to reduce the contribution of non-faradic current to the current of polarization curves. The series resistance (R_s), mainly originated from ionic conduction in the electrolyte, is in the range of 5.0 to 7.0 Ω.

2 Detailed model descriptions

2.1 Scaling relation used for kinetic simulation

The intermediates in our kinetic model are kinetic-relevant reaction intermediates, which should be distinguished from underpotential deposited species.[7-9] Based on the definition of equilibrium potential used in our kinetic model, the scaling relation needs to be modified to well describe kinetics for multi-step irreversible reactions. Based on a number of experimental results from both literature and our laboratory, we find the parameters in scaling relation[10-11] that can well describe experimental trends.

$$\Delta G_{\mathrm{OOH}^*} - \Delta G_{\mathrm{OH}^*} = 2.8 \text{ eV} \quad (1)$$

$$\Delta G_{\mathrm{O}^*} = 1.65 * \Delta G_{\mathrm{OH}^*} + 0.58 \text{ eV} \quad (2)$$

2.2 Adsorption isotherm

If the adsorption step of a reactive intermediate is too much faster than the subsequent step, the intermediate adsorption could be treated as in equilibrium step. Due to interaction among the adsorbed intermediate, the adsorption free energy also varies with intermediate coverage, especially at high coverage.[12]

$$\Delta G^{0\prime} = \Delta G^{0} + c\theta \quad (3)$$

where θ is dimensionless and c describes the rate of change of adsorption free energy with coverage, thus c has the same unit as ΔG. This equation is a general description of intermediate adsorption. When c is small enough (approaching 0), it becomes Langmuir adsorption isotherm; when c is significantly higher than 0, it becomes Temkin isotherm. The coverage of intermediate can only be calculated by numerical methods for Temkin adsorption.

In our modeling of experimental kinetics, we first try the Langmuir adsorption isotherm. We tend to adopt the result of Langmuir adsorption isotherm once we can get a satisfactory fitting result with it. For the Temkin isotherm, it only exerts significant influence of kinetic curves over the coverage range of 0.2 ~ 0.8, which corresponds to the potential range beyond the onset potential. If the simulation results based on the Langmuir adsorption isotherm only show significant deviation from experimental kinetics at relatively high coverage of intermediates, we use the Temkin isotherm to peruse better fitting results. However, it should be noted that using the two effects to simulate the same kinetics can return same energy profile.

2.3 Reaction rate law for OER

Since both OER and ORR are highly irreversible reactions, the back reaction of RDS is neglected, while the rest steps remain in quasi-equilibrium. Here we use i = 1, 2, 3 referring to RDS is the first, second, third electron-transfer (ET) step for OER. Besides, we use i = 1.5, 2.5 to describe the chemical reaction RDS between ET steps to formulate a general description.

Our purpose of such naming for the chemical step is to give a general description of Tafel slope for electron transfer steps and chemical steps (equation (4)). OER is a multi-electron transfer process – four electrons transferred per O_2 generated. However, besides the electron transfer step, purely chemical step (no electron transfer occurred) may also be involved in the catalytic cycle. The chemical reactions are proposed to account for the typical Tafel slope of 60 mV/dec or 30 mV/dec.[13]

$$b = \frac{2.3\,RT}{(n+\alpha-1)F} = \frac{60}{n+\alpha-1}\,\mathrm{mV/dec} \qquad (4)$$

According to previous kinetic analysis,[13-14] the step 1.5 and 2.5 probably refer to:

$$\mathrm{M-OH*} + \mathrm{OH^-} \rightleftarrows \mathrm{M-O^-} + \mathrm{H_2O} \qquad (\mathrm{n = 1.5}) \qquad (5)$$

$$\mathrm{M-O*} + \mathrm{OH^-} \rightleftarrows \mathrm{M-OOH^-} \qquad (\mathrm{n = 2.5}) \qquad (6)$$

$i = 4$ is least possible in OER, thus we ignore its kinetics here. The elementary steps of OER and ORR are shown in Scheme S1:

For $i = 1$, the velocity of RDS is given by:

$$v_1 = k_1\,\theta_{\mathrm{M}^*}\,a_{\mathrm{R}} \qquad (7)$$

where θ_{M^*} represents the surface coverage of empty catalytic sites, which is 1 for this case. a_{R} is the activity of reactant, which is OH^- in alkaline and H_2O in acid.

For $i = 2$ and 3, velocity of RDS is given by:

$$v_2 = k_2\,\theta_{\mathrm{OH}^*}\,a_{\mathrm{R}} \qquad (8)$$

$$v_3 = k_3\,\theta_{\mathrm{O}^*}\,a_{\mathrm{R}} \qquad (9)$$

θ_{OH^*} and θ_{O^*} represent the surface coverage of OH* and O*.

For $i = 1.5$ and 2.5, velocity of RDS is given by:

$$v_{1.5} = k_{1.5}\,\theta_{\mathrm{OH}^*} \qquad (10)$$

$$v_{2.5} = k_{2.5}\,\theta_{\mathrm{O}^*} \qquad (11)$$

where $k_{1.5}$ and $k_{2.5}$ are reaction rate constants for the chemical reaction. Different from the reaction rate constants of ET steps, that for pure chemical reaction is independent on potential.

From equation (10) and (11) we can understand that, for the catalysts whose RDS is chemical reaction, the kinetics is only determined by the surface coverage of intermediates with a given reaction rate constant.

For i = 1.5 and 2, the active sites are either empty or occupied by OH*.

$$\theta_{\mathrm{M}^*} + \theta_{\mathrm{OH}^*} = 1 \qquad (12)$$

Strictly speaking, only the sum of all adsorbed species and empty active sites amounts to 1. However, the calculation would be very time-consuming if the relative coverage of O* and OOH* are very small, while neglection of these species would not cause significant difference. Therefore, this is a common approximation for the second step being RDS in OER, which is for the ease of calculation.[13, 15] The sum coverage of M* and OH* equals to unity only apply for cases where the second step as RDS, which is O* formation from OH*. For this situation, the following steps (the generation and consumption of O* and OOH*) are fast. Under the potential where OER could occur, all the steps become downhill in energy (Figure 1). Since the real concentration of dissolved O_2 is very low (on the order of 10^{-3} mol/L),[16] the quantity of O* and OOH* should be extremely low even under equilibrium with dissolved O_2. Therefore, the relative surface coverage can be neglected in kinetic analysis as kinetic equations are described based on major species.[13, 15] The validity of this approximation is also supported by the recent work by Koper *et al*,[17] who demonstrated that the dissolved O_2 in electrolyte has no significant effect on the kinetics of OER catalysts except for the bubbles formation on electrodes. The significant lower kinetics should be expected for OER catalysts in O_2 saturated electrolyte if O* and OOH* occupy a significant coverage of active sites.

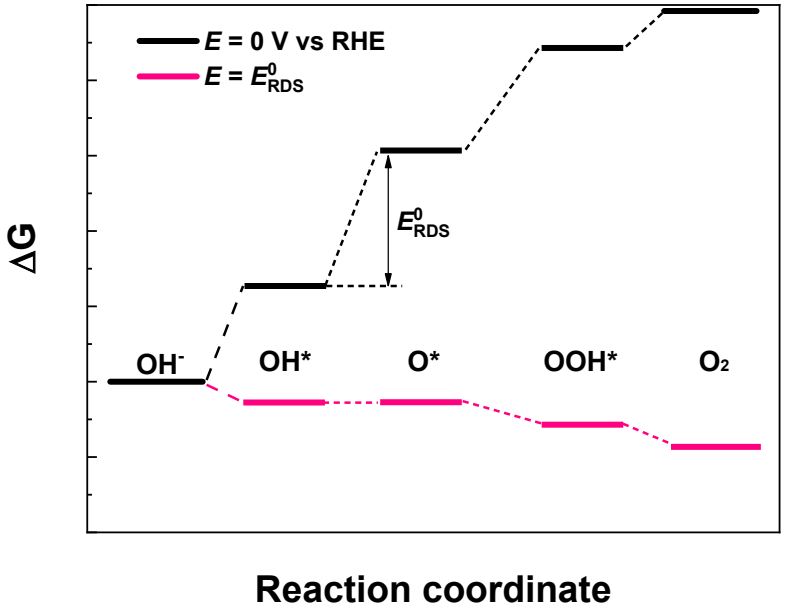

Figure S1. Schematic energy diagram for a typical OER catalyst with second step as RDS and PDS. The energy profile for electrochemical reactions are dependent on the applied potential. Although under the potential of RHE all steps are uphill, all the steps except for RDS become downhill under the applied potential reaching E^0_{RDS}. Therefore, two equilibrium will be formed: one is between reactant with OH*, the other is between O*, OOH* and solved O_2 in electrolyte. From the energetic aspect, the equilibrium favours OH* formation under OER working potential but disfavours O* and OOH*. Moreover, from the concentration of reactant OH^- or H_2O (for acidic and neutral OER) is above three orders higher than solved O_2. Thus, the two factors together would support our approximation.

Since adsorption of OH^* is the equilibrium step, reaction (1) as shown in Scheme S1 is in equilibrium.

$$\frac{\theta_{\mathrm{OH}*}}{\theta_{\mathrm{M}*}a_{\mathrm{OH}-}} = K_1^0 e^{\frac{F(E-E_1^0-c_1\theta_{\mathrm{OH}*})}{RT}} \qquad (13)$$

where K_1^0 is equilibrium constant of reaction (1) under the potential equals to E_1^0. c_1 becomes zero for Langmuir adsorption.

From equation (9) and (10) we can get:

$$\theta_{\mathrm{OH}^*} = 1 - \frac{1}{1 + K_1^0 e^{\frac{F(E - E_1^0 - c_1\theta_{\mathrm{OH}^*})}{RT}}} \quad (14)$$

Since the right side of equation (14) also contains θ_{OH^*} for Temkin isotherm, the equation can only be solved numerically.

For i = 2.5 and 3,

$$\theta_{\mathrm{M}^*} + \theta_{\mathrm{OH}^*} + \theta_{\mathrm{O}^*} = 1 \quad (15)$$

Reaction (2) is also in equilibrium.

$$\frac{\theta_{\mathrm{O}^*}}{\theta_{\mathrm{OH}^*} a_{\mathrm{OH}^-}} = K_2^0 e^{\frac{F(E - E_2^0)}{RT}} \quad (16)$$

and

$$\theta_{\mathrm{O}^*} = \frac{K_1^0 K_2^0 e^{\frac{F(2E - E_1^0 - E_2^0)}{RT}}}{1 + K_1^0 e^{\frac{F(E - E_1^0)}{RT}} + K_1^0 K_2^0 e^{\frac{F(2E - E_1^0 - E_2^0)}{RT}}} \quad (17)$$

For dissociative pathway, only the O_2 generation step is different from the associative pathway. If the O_2 generation step is the RDS,

$$v_{3'} = k_{3'} \theta_{\mathrm{O}^*}{}^2 \quad (18)$$

where $k_{3'}$ is the reaction rate constant and independent of potential due to no ET step. θ_{O^*} here shares the same description as in the associative pathway.

2.4 Reaction rate law for ORR

The kinetic description of our model is shown in Scheme S1, where step (1) and (4) are key steps that determine the kinetic fingerprint of ORR.[18-20] The fundamental difference of the two mechanisms would result in different trend of the surface coverage of OH* with potential: θ_{OH^*} decreases with overpotential of ORR for the mechanism of Scheme S1 A, while θ_{OH^*} increases for the other mechanism.

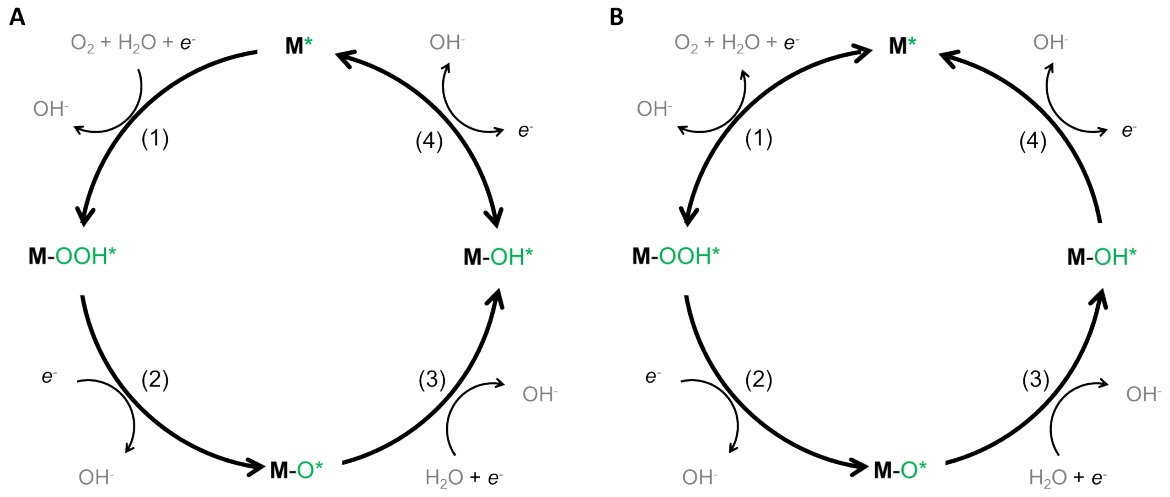

Scheme 1. Reaction mechanism of ORR. (*A*) O_2 hydrogenation is RDS while OH* reduction is in quasi-equilibrium. This mechanism is used to simulate the kinetics of Pt group catalysts and the catalysts with weak surface reactivity. (*B*) OH* reduction is RDS while O_2 hydrogenation is in quasi-equilibrium. This mechanism is mainly suitable for the catalysts onto which oxygen intermediates adsorb too strongly (on the strong binding leg of volcano plot).

For the mechanism as shown in Scheme S1 A, the velocity of overall reaction is described as:

$$v_1^{\mathrm{ORR}} = k_1^{\mathrm{ORR}}\,\theta_{\mathrm{M}^*}\,a_{\mathrm{O}_2} \qquad (19)$$

where a_{O_2} is the activity of dissolved O_2 in saturated electrolyte, which is dependent on type of electrolyte and concentration.[16]

The rate constant is given by,

$$k_1^{\mathrm{ORR}} = k_1^{\mathrm{ORR},0} * e^{\frac{-\alpha F(E - E_1{}^0)}{RT}} \qquad (20)$$

The surface coverage of active site M* is given by:

$$\theta_{\mathrm{M}^*} = \frac{1}{1 + K_4^0 e^{\frac{-F(E - {E_4}^0 - c\theta_{\mathrm{OH}^*})}{RT}}} \quad (21)$$

For the mechanism as shown in Scheme S1 B, the velocity and surface coverage of OH* are described as:

$$v_4^{\mathrm{ORR}} = k_4^{\mathrm{ORR}}\, \theta_{\mathrm{OH}^*} \quad (22)$$

$$\theta_{\mathrm{OH}^*} = 1 - \frac{1}{1 + K_4^0 e^{\frac{-F(E - {E_1}^0)}{RT}}} \quad (23)$$

Our above kinetic model for ORR is based on the formally neutral intermediates. However, another possible mechanism based on the charged intermediates (Scheme 2A) are also widely used to account for the high ORR activity in alkaline media.[21-22] A summarized comparison between the charged and neutral intermediates mechanism l is shown in Scheme 2. Although the molecular structure is different, the oxygen redox is almost the same for the two mechanisms. The major dispute lies in the molecular structure of the intermediates, i.e., whether they are negatively charged (deprotonated form of OOH* and OH*) or remain neutral. Regarding this issue, we think it maybe not strictly one way or the other. The adsorption of the intermediates may result in a charge distribution between adsorbates and substrate. Therefore, the intermediates are usually partially charged, such as $OH^{\delta-}$ on gold.[23] The electronic structure of oxygen intermediates may differ on different catalysts due to the different bonding strength. Therefore, in this work we would like to emphasize the **formal oxidation state** of oxygen intermediates to visualize the oxygen redox involved in oxygen electrocatalysis. To emphasize the uncertainty of electronic structure of oxygen intermediates, we gave a statement over this issue in the figure caption. Therefore, we think the both forms should be acceptable as no solid evidences to exclude neither situation.

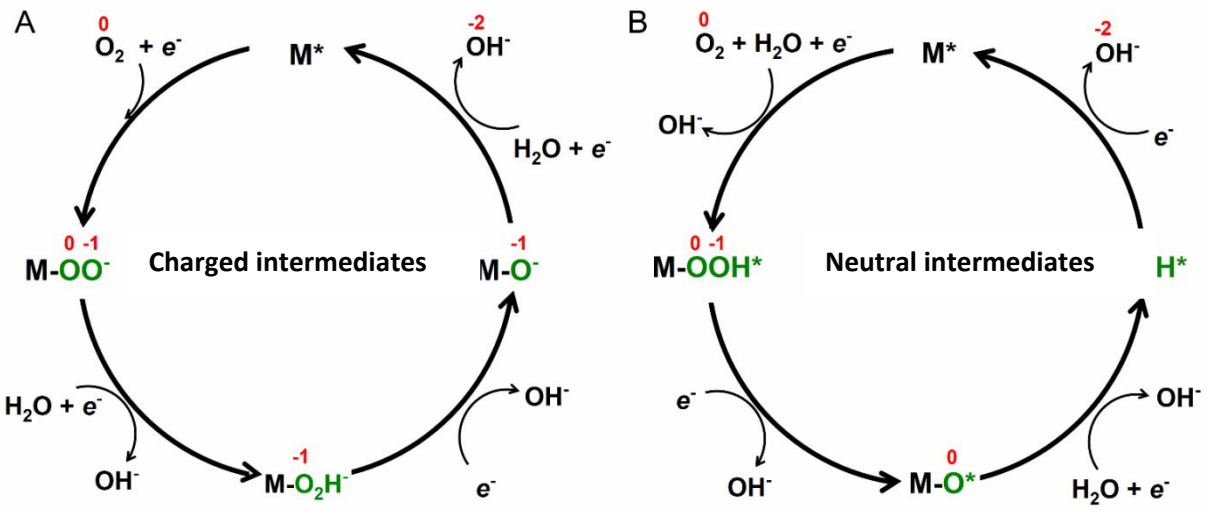

Scheme 2. Comparison of the reaction mechanism based on charged and neutral intermediates of our work. (*A*) The mechanism of 4 e^- ORR based on charged intermediates. (*B*) The reaction mechanism proposed in our original manuscript.

2.5 Current density

For both OER and ORR, the absolute value of steady state current density of the overall reaction is described by:

$$J_{\mathrm{ET}} = 4Fv_i \tag{24}$$

The above formulation only considers pure kinetic limitation. When reaction rate increases, mass transport limitation will become increasingly significant. The overall reaction rate is proportional to the steady state current density (*J*) that can be readily measured by potentiostat equipment. *J* is given by:

$$\frac{1}{J} = \pm\left(\frac{1}{J_{\mathrm{MT}}} + \frac{1}{J_{\mathrm{ET}}}\right) \tag{25}$$

The simulated current should be positive for OER but negative for ORR due to electron-transfer direction. Note: J_{MT} is constant at a given reaction condition such as reactant concentration, active catalyst surface area and rotating rate for RDE tests.

3 Details for kinetic simulation and modeling

3.1 Error analysis and experimental data criteria

As the electrochemical kinetics are influenced by both electronic and geometric factors,[24] here we give our definition of error bars in the adsorption energy obtained from kinetic modeling. As shown in equation (26), the energy of intermediates in our kinetic model, which are described by E_i^0, are mainly determined by electronic factor. The electronic factor can be influenced by defects and crystal facets. On the other hand, the geometric factors such as particle size or morphology (providing such variation do not cause difference of electronic change) influence kinetics by changing k_i^0. A kinetic simulation shown in Figure S1 visualizes the different influence of the two different factors.

$$k_i = k_i^0 * e^{\frac{\alpha F(E - E_i^0)}{RT}} \quad (26)$$

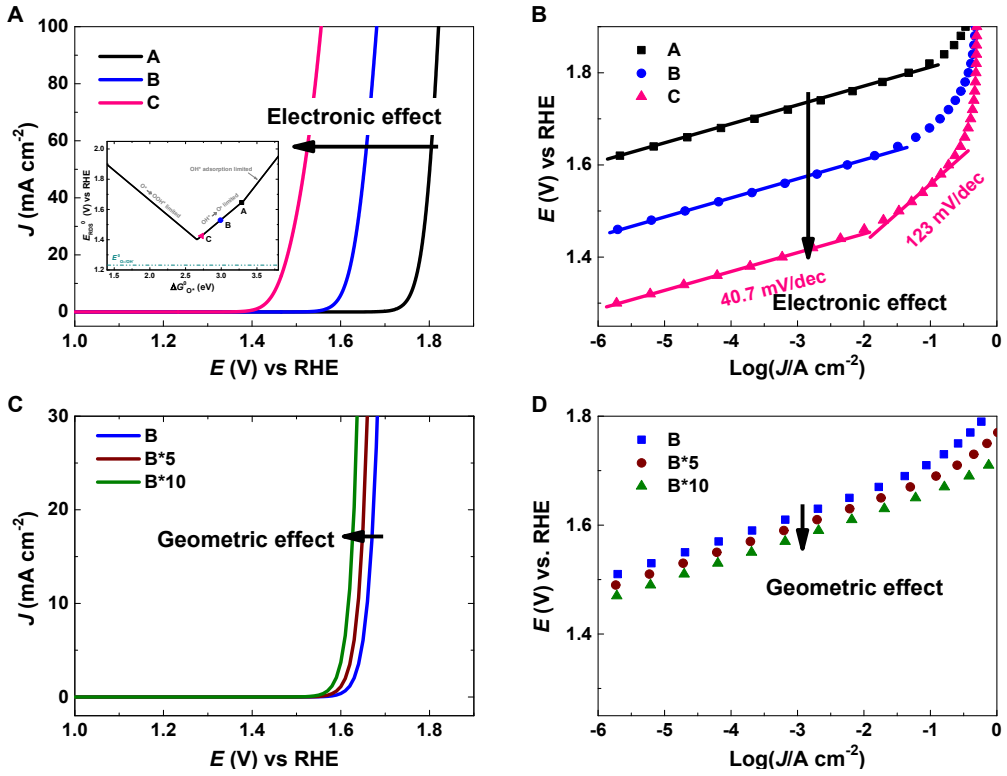

Figure S2. Different influence of electronic and geometric factors on OER kinetics. (*A,B*) Simulated LSVs and Tafel plots influenced by surface reactivity (electronic factor). Inset shows the position of the simulated catalysts in the activity volcano plot. Hundreds of mV overpotential change can be achieved by tuning surface reactivity. (*C,D*) Simulated LSVs and Tafel plots influenced by improved surface area (geometric difference). The improved surface area with one order of magnitude only reduces tens of mV reduction in overpotential.

As shown in Figure S2, the change of intermediates energetics gives rise to distinctive fingerprints in kinetics, such as variation of Tafel slope and intermediates coverage as a function of potential. On the contrary, pure geometric difference, which results in different active surface area, can only influence the total current, instead of TOF.

Several parameters are involved in kinetic equations, which makes kinetic fitting very difficult. In particular, in the kinetic equation, k^0_i and E^0_i are coupled. However, some parameters can be defined to correlate with kinetic fingerprints. One of the most obvious kinetic fingerprints is the onset potential in the *J-V* curve. In our model, we take the onset potential as the initial value of the equilibrium potential of RDS in iterative calculations. This definition can be validated from the ideal case, where OER and ORR are reversible. Although the ideal case does not exist, we can take it as a boundary condition. For the reversible oxygen catalyst, E^0_i (i = 1, 2, 3, 4) equals to 1.23 V. The sum of E^0_i of the four concerted electron transfer step is 4.92 V. Significant Faradaic current will appear when applied potential is higher (lower) than E^0_i for OER (ORR). When this definition extends to the irreversible situation, the irreversibility in this model and many DFT calculations are rationalized by the mismatch of the E^0_i of elementary steps, wherein the step with the highest thermodynamic barrier results in overpotential.[10-11, 25-26] Therefore, based on this definition, when applied potential is higher (lower) than E^0_i of RDS in OER (ORR), significant Faradaic current appears. The reaction intermediates described in our model are kinetic-relevant intermediates. Thus, significant Faradaic current would emerge from the low coverage of the reactive intermediates for RDS. Therefore, we use the onset potential for the formation of the intermediates to derive their binding energies.

To enable the automatic fitting of experimental data using a programme, we must fix either the value of k^0_i or E^0_i. To improve the accuracy of modeling, we fix the value of k^0_i in kinetic fitting as the value of k^0_i can be estimated by electrochemical active surface area (ECSA). The k^0_i for IrO_2 is set as $10*10^{-8}$ s^{-1}, while the k^0_i for other catalysts is obtained by normalized ECSA. However, so far, we have not obtained experimental evidence to support our assumed value of k^0_i. The empirical value is necessary to fulfil the activity trend, similar with the treatment of k^0 in Norkov's paper.[27]

Since different catalysts have different surface areas, the k^0_i values for catalysts with very different surface areas may differ significantly. To address this issue, we use ECSA to estimate k^0_i of different catalysts. The data determination of ECSA and results are shown in Figure S3 and Table 1.

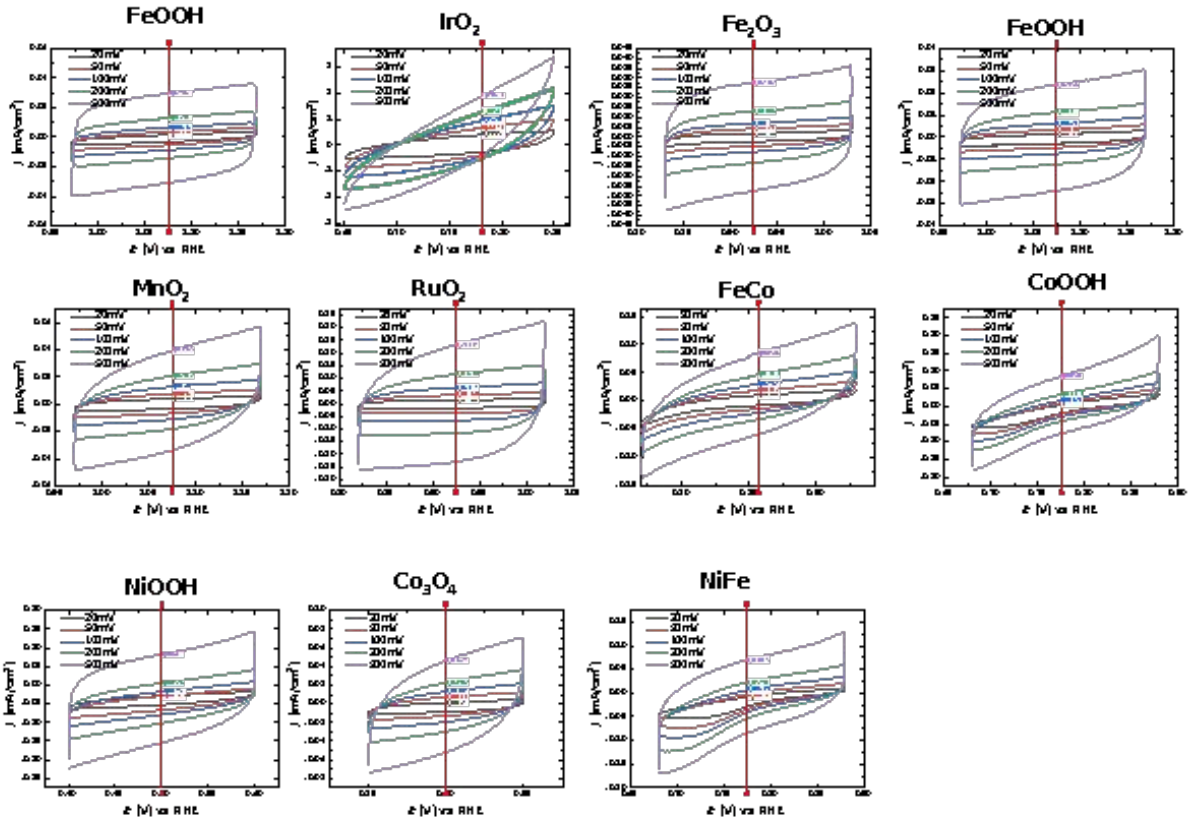

Figure S3. The CV curves for the calculation of ECSA.

Table 1. The determined ECSA and value of k^0_i.

Catalyst	**Capacitance / F cm^{-2}**	$\boldsymbol{k^0_i}$
FeOOH	5.82E-05	2.01E-09
IrO_2	0.00289	1.00E-07
Fe_2O_3	5.32E-05	1.84E-09
TiO_2	4.54E-05	1.57E-09
MnO_2	7.20E-05	2.49E-09
RuO_2	4.48E-04	1.55E-08
FeCo	1.51E-04	5.24E-09
CoOOH	1.70E-04	5.89E-09
NiOOH	2.39E-04	8.28E-09
Co_3O_4	9.00E-05	3.11E-09
NiFe	1.62E-04	5.60E-09

3.2 Kinetic simulation

Here we provide details of the simulation results for different cases.

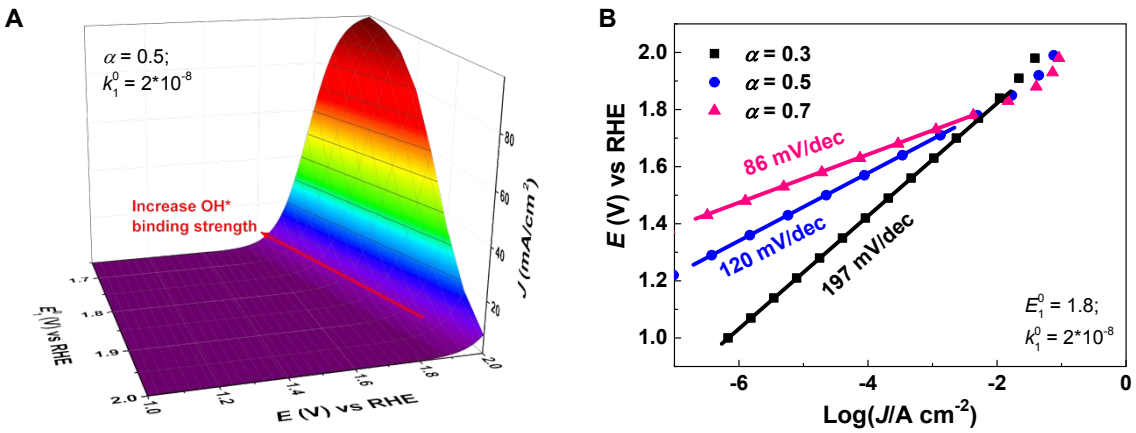

Figure S4. Influence of OER kinetics by key factors (i = 1). (A) Influence of equilibrium potential ($E_1{}^0$). In this case, the surface reactivity is too low to adsorb OH*. Therefore, increasing OH* bonding strength on such catalyst should be an effective way to reduce overpotential. (B) Influence of transfer coefficient on Tafel plots. Transfer coefficient has a significant influence on Tafel slope and thus overpotential. Therefore, for such catalysts, Tafel slope may deviate greatly from the typical value of 120 mV/dec (see the example of TiO_2 in our previous work[1]).

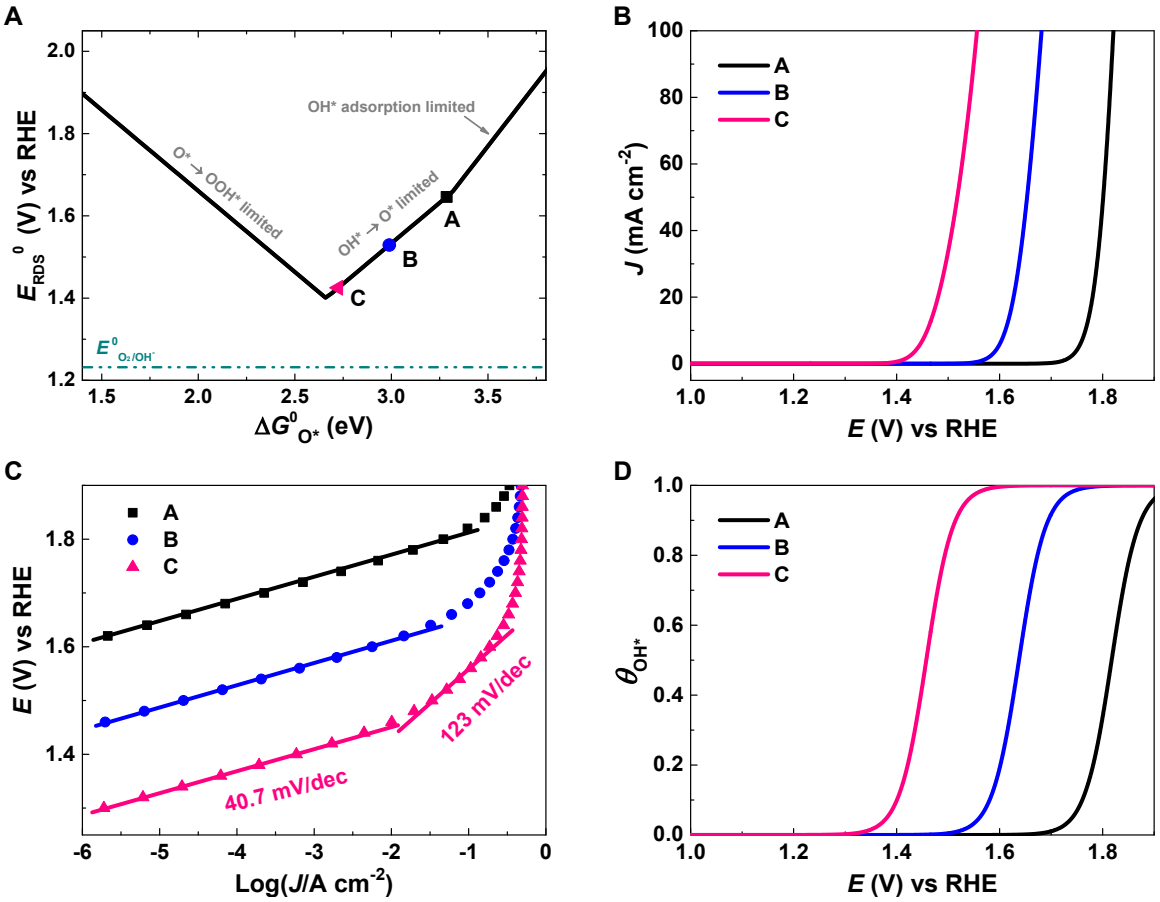

Figure S5. Kinetic modeling of OER kinetics as a function of key factors ($i = 2$). (*A*) Simulated LSV curves of OER catalysts. (*B*) Simulated LSV curves of the catalysts as shown in the volcano plot. (*C*) Tafel plots. (*D*) Variation of θ_{OH^*} as a function of potential.

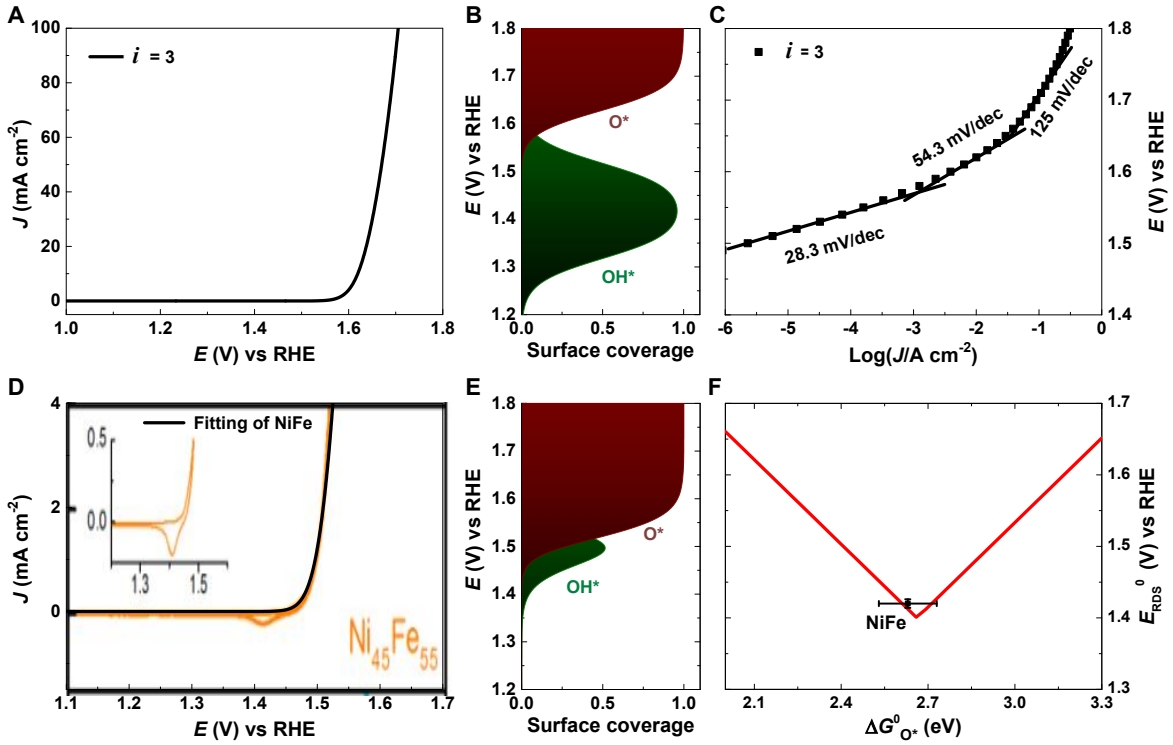

Figure S6. Kinetic modeling of OER kinetics ($i = 3$). (*A, B, C*) Simulated LSV curve, surface coverage of intermediates and Tafel plot. (*D, E, F*) Modeling of kinetics of NiFe catalysts reported by Strasser *et al*.[28]

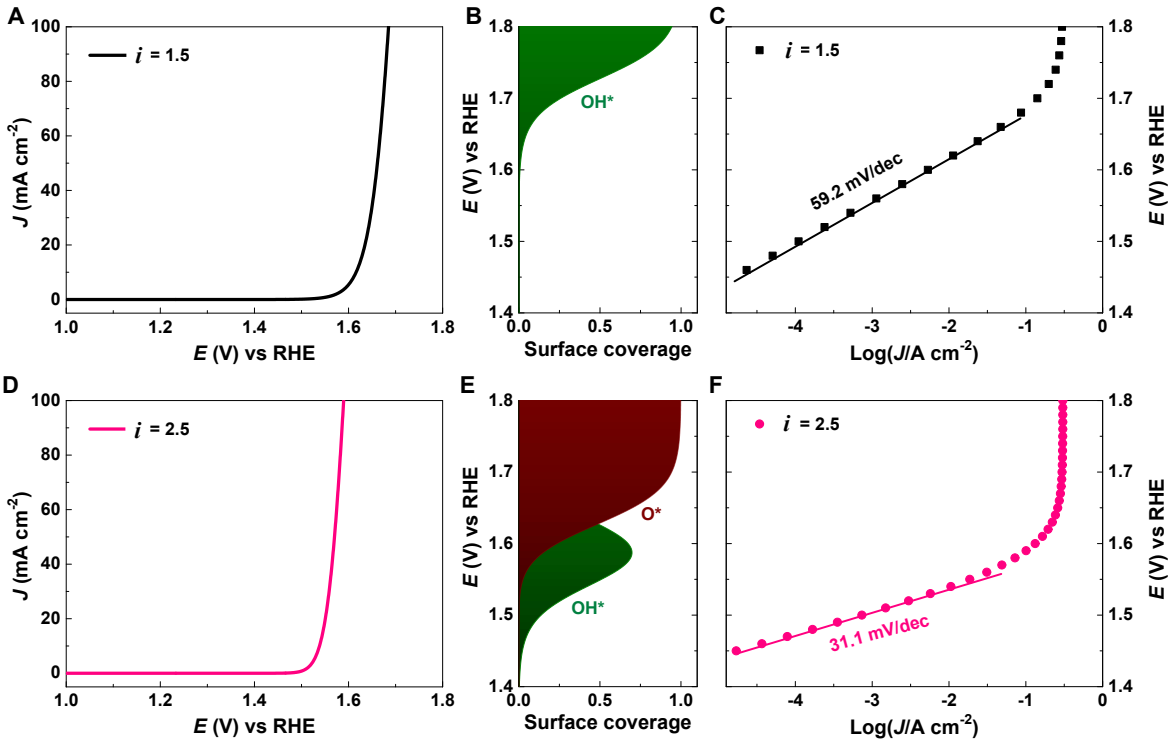

Figure S7. Kinetic modeling of OER kinetics for chemical reaction as the RDS (i = 1.5, 2.5). (*A, B, C*) Simulated LSV curve, OH* coverage and Tafel plot for n = 1.5 (the chemical reaction after OH* generation). (*A, B, C*) Simulated LSV curve, OH* coverage and Tafel plot for i = 2.5 (the chemical reaction after O* formation).

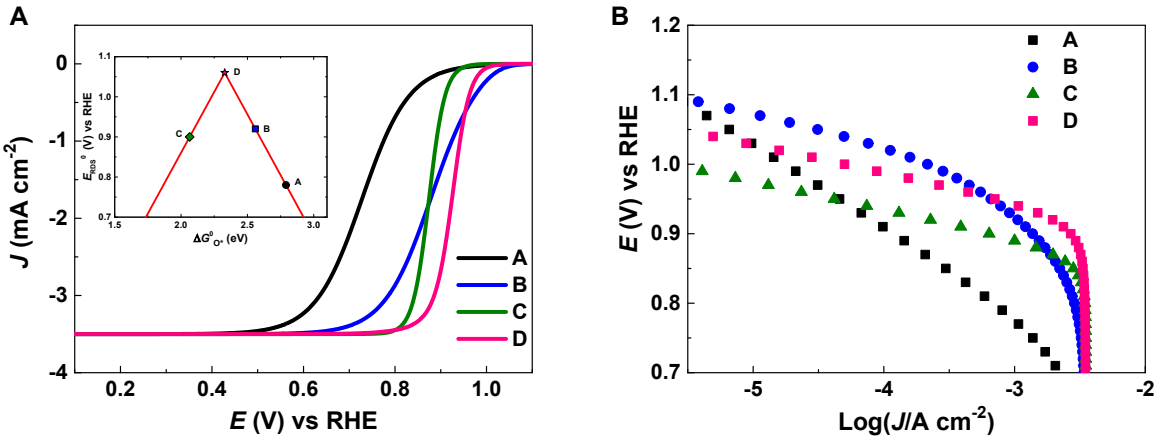

Figure S8. Kinetic modeling of ORR catalysts as shown in the volcano plot. (*A*) Simulated LSV curves. (*B*) Simulated Tafel plots. Simulated LSV curves and Tafel plots for the catalysts on the right side of volcano plot well reproduce the basic features commonly observed in experimental data: the polarization is serious due to high Tafel slope, such as Au, Ag and many metal oxides. Whereas, for the catalysts on the left side, the Tafel slope is relatively smaller, which is consistent with the data reported in literature that typical Tafel slopes (40~60 mV/dec) for Pt, Pd based catalysts are at low overpotential.

3.3 Kinetic modeling of catalysts

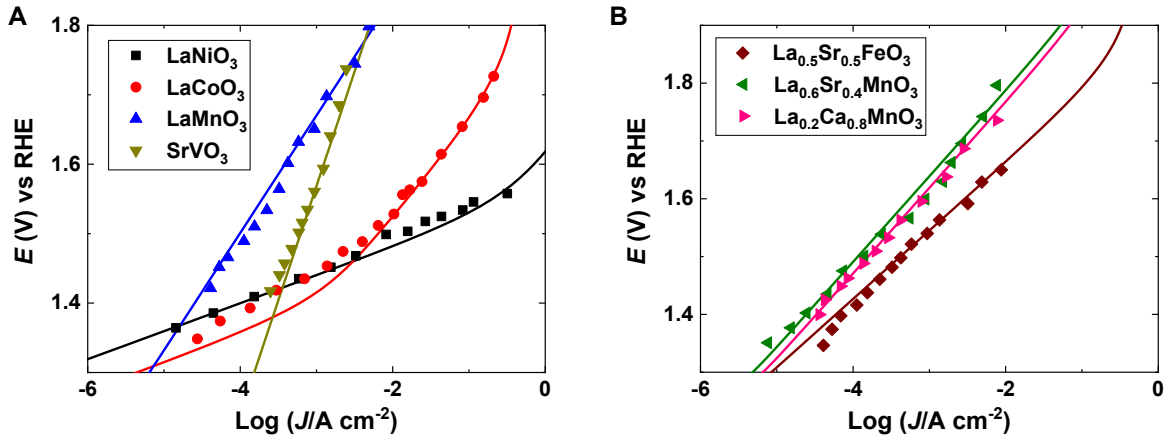

Figure S9. Kinetic modeling of OER kinetics of perovskite oxides from literature.[23] $LaMnO_3$ and its doped oxides all show high Tafel slope and poor OER activity, which may be resulted from both too weak and too strong binding energy. The conclusive assignment of surface reactivity needs to take consideration of their kinetics in ORR. As we discussed in the main text, the catalysts belong to weak binding side of OER volcano plot tend to show very poor ORR activity, whereas the strong binding OER catalysts can show relatively good ORR activity. The kinetic feature in OER and ORR fit the latter case and thus are assigned to the strong binding leg in activity volcano plot (Figure 3 in main text).

In our modeling of experimental kinetics, we take the onset potential as the initial value of E^0_{RDS}, while the range for the optimization of E^0_{RDS} is restricted within 100 mV of the onset potential. In the procedure of kinetic modeling, the best fitting is defined as the smallest r.m.s. error of [$\log(J_{fitting})$ - $\log(J_{exp})$]. The selected experimental data for fitting should consist of mainly Faradaic current, thus the capacitance charging current should be minimized or reduced. Therefore, the steady state *J*-*V* curve (converted to $\log(J)$ vs E) is preferable. Since oxygen electrocatalysis is very irreversible, the data falling in the potential range where no Faradaic current appears is omitted in the kinetic fitting.

Considering the scaling relationship of oxygen binding energies, the potential range choose for fitting is summarized in Table 2. A small potential range overlap is used to account for the possible error in experimental tests and fitting.

Table 2. Potential range used in modeling for different step being RDS.

Reaction	**RDS**	E^0_1 **(V)**	E^0_2 **(V)**	E^0_3 **(V)**
OER	$i = 1$	1.62 ~ 2.10	-	-
	$i = 2$	1.23 ~ 1.67	1.38 ~ 1.70	-
	$i = 3$	0.28 ~ 1.30	0.70 ~ 1.41	1.41 ~ 2.10
	RDS	E^0_1 **(V)**	E^0_4 **(V)**	
ORR	$i = 1$	0 ~ 1.06	1.06 ~ 2.12	
	$i = 4$	1.06 ~ 2.12	0 ~ 1.06	

The following figures (not numbered) show the fitting results analysis by *origin pro* programme. The uncertainty (sensitivity analysis) of the kinetic parameters are provided in each figure.

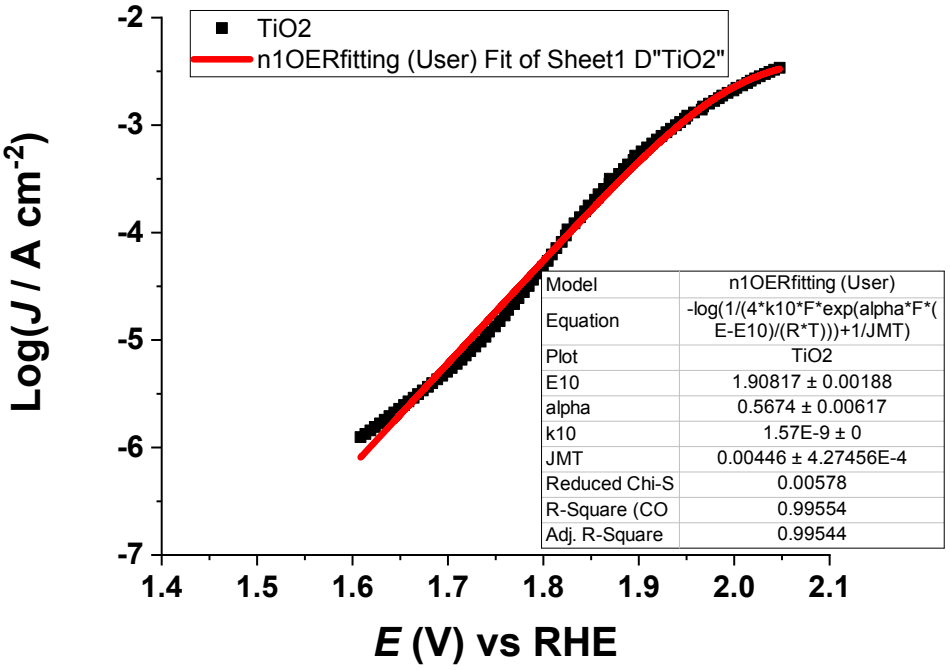

Model	n1OERfitting (User)
Equation	-log(1/(4*k10*F*exp(alpha*F*(E-E10)/(R*T)))+1/JMT)
Plot	TiO2
E10	1.90817 ± 0.00188
alpha	0.5674 ± 0.00617
k10	1.57E-9 ± 0
JMT	0.00446 ± 4.27456E-4
Reduced Chi-S	0.00578
R-Square (CO	0.99554
Adj. R-Square	0.99544

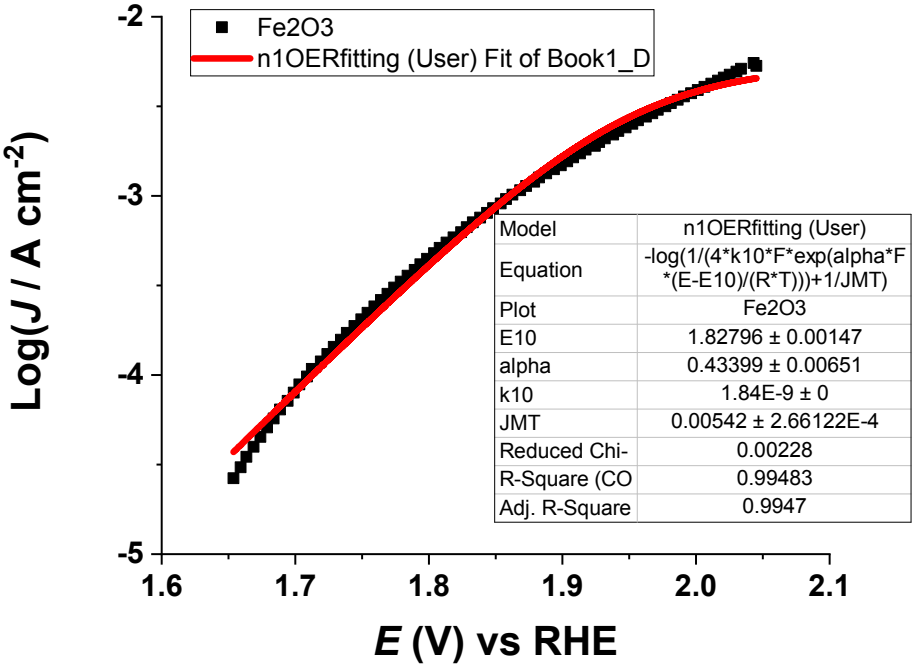

Model	n1OERfitting (User)
Equation	-log(1/(4*k10*F*exp(alpha*F*(E-E10)/(R*T)))+1/JMT)
Plot	Fe2O3
E10	1.82796 ± 0.00147
alpha	0.43399 ± 0.00651
k10	1.84E-9 ± 0
JMT	0.00542 ± 2.66122E-4
Reduced Chi-	0.00228
R-Square (CO	0.99483
Adj. R-Square	0.9947

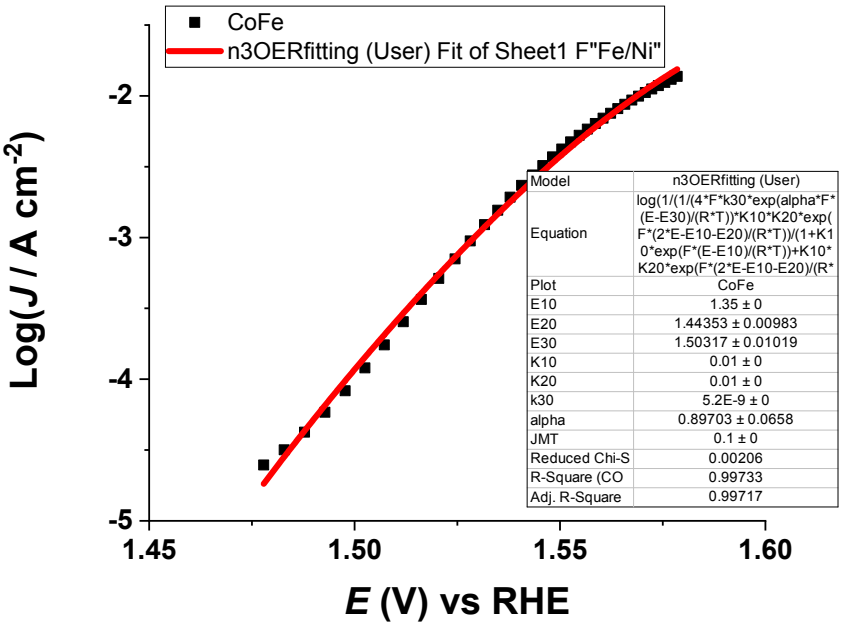

Model	n3OERfitting (User)
Equation	log(1/(1/(4*F*k30*exp(alpha*F*(E-E30)/(R*T))*K10*K20*exp(F*(2*E-E10-E20)/(R*T))/(1+K10*exp(F*(E-E10)/(R*T))+K10*K20*exp(F*(2*E-E10-E20)/(R*
Plot	CoFe
E10	1.35 ± 0
E20	1.44353 ± 0.00983
E30	1.50317 ± 0.01019
K10	0.01 ± 0
K20	0.01 ± 0
k30	5.2E-9 ± 0
alpha	0.89703 ± 0.0658
JMT	0.1 ± 0
Reduced Chi-S	0.00206
R-Square (CO	0.99733
Adj. R-Square	0.99717

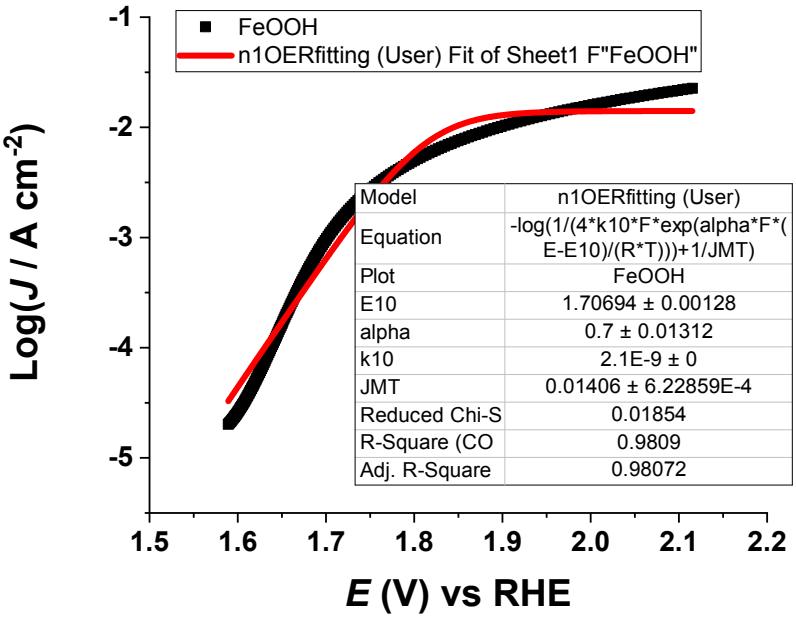

Model	n1OERfitting (User)
Equation	-log(1/(4*k10*F*exp(alpha*F*(E-E10)/(R*T)))+1/JMT)
Plot	FeOOH
E10	1.70694 ± 0.00128
alpha	0.7 ± 0.01312
k10	2.1E-9 ± 0
JMT	0.01406 ± 6.22859E-4
Reduced Chi-S	0.01854
R-Square (CO	0.9809
Adj. R-Square	0.98072

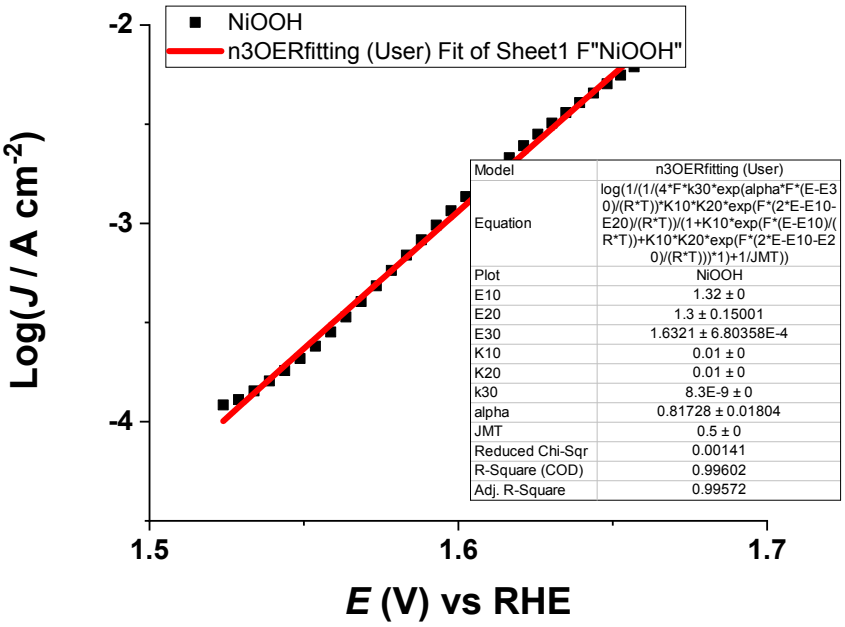

Model	n3OERfitting (User)
Equation	log(1/(1/(4*F*k30*exp(alpha*F*(E-E30)/(R*T))*K10*K20*exp(F*(2*E-E10-E20)/(R*T))/(1+K10*exp(F*(E-E10)/(R*T))+K10*K20*exp(F*(2*E-E10-E20)/(R*T)))*1)+1/JMT))
Plot	NiOOH
E10	1.32 ± 0
E20	1.3 ± 0.15001
E30	1.6321 ± 6.80358E-4
K10	0.01 ± 0
K20	0.01 ± 0
k30	8.3E-9 ± 0
alpha	0.81728 ± 0.01804
JMT	0.5 ± 0
Reduced Chi-Sqr	0.00141
R-Square (COD)	0.99602
Adj. R-Square	0.99572

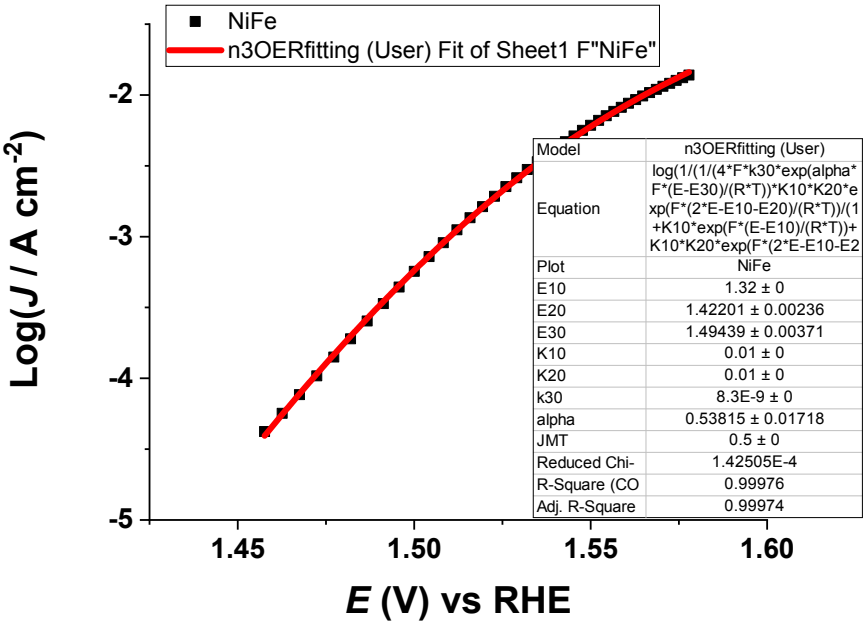

Model	n3OERfitting (User)
Equation	log(1/(1/(4*F*k30*exp(alpha*F*(E-E30)/(R*T))*K10*K20*exp(F*(2*E-E10-E20)/(R*T))/(1+K10*exp(F*(E-E10)/(R*T))+K10*K20*exp(F*(2*E-E10-E2
Plot	NiFe
E10	1.32 ± 0
E20	1.42201 ± 0.00236
E30	1.49439 ± 0.00371
K10	0.01 ± 0
K20	0.01 ± 0
k30	8.3E-9 ± 0
alpha	0.53815 ± 0.01718
JMT	0.5 ± 0
Reduced Chi-	1.42505E-4
R-Square (CO	0.99976
Adj. R-Square	0.99974

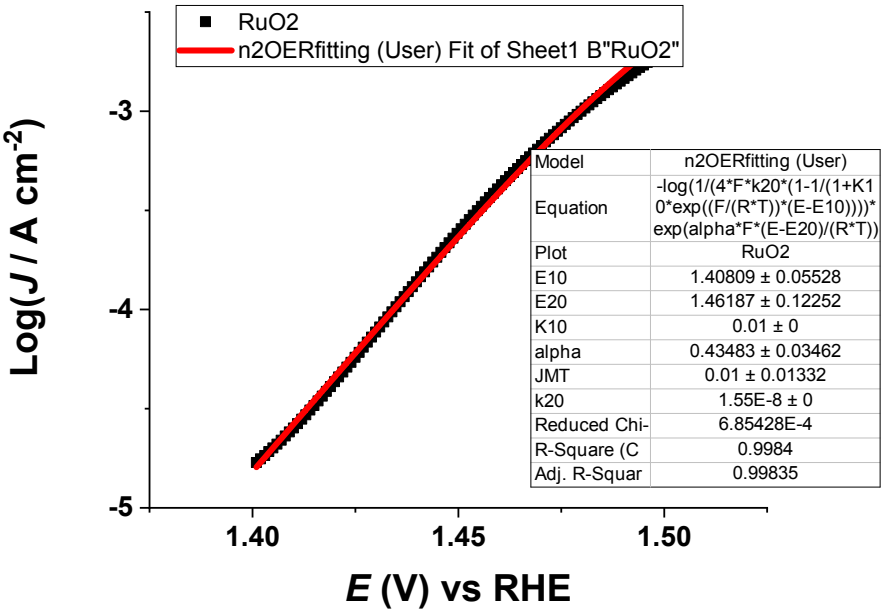
RuO2
n2OERfitting (User) Fit of Sheet1 B"RuO2"
Log(J / A cm-2)
-3
-4
-5
1.40
1.45
1.50
E (V) vs RHE
Model n2OERfitting (User)
Equation -log(1/(4*F*k20*(1-1/(1+K10*exp((F/(R*T))*(E-E10))))*exp(alpha*F*(E-E20)/(R*T))
Plot RuO2
E10 1.40809 ± 0.05528
E20 1.46187 ± 0.12252
K10 0.01 ± 0
alpha 0.43483 ± 0.03462
JMT 0.01 ± 0.01332
k20 1.55E-8 ± 0
Reduced Chi- 6.85428E-4
R-Square (C 0.9984
Adj. R-Squar 0.99835

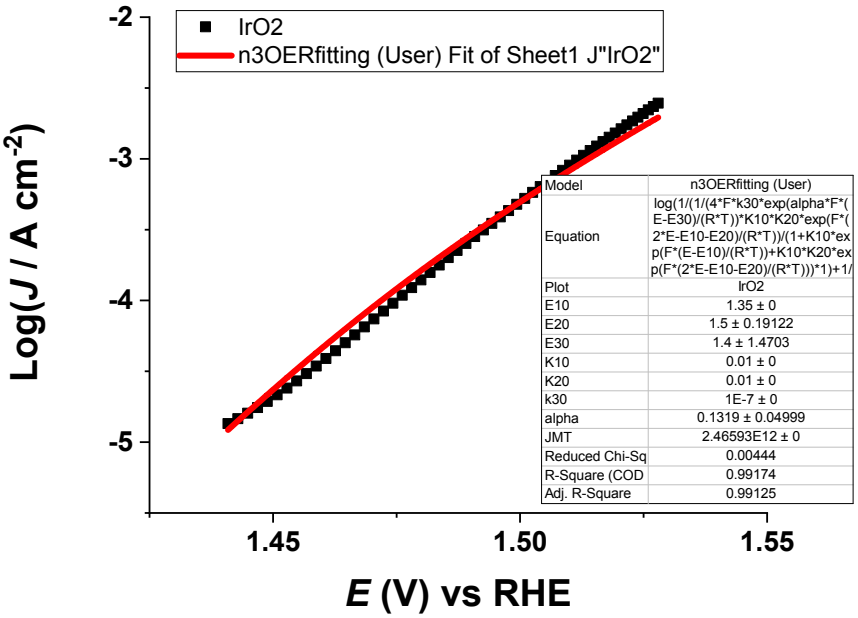
IrO2
n3OERfitting (User) Fit of Sheet1 J"IrO2"
Log(J / A cm-2)
-2
-3
-4
-5
1.45
1.50
1.55
E (V) vs RHE
Model n3OERfitting (User)
Equation log(1/(1/(4*F*k30*exp(alpha*F*(E-E30)/(R*T))*K10*K20*exp(F*(2*E-E10-E20)/(R*T))/(1+K10*exp(F*(E-E10)/(R*T))+K10*K20*exp(F*(2*E-E10-E20)/(R*T)))*1)+1/
Plot IrO2
E10 1.35 ± 0
E20 1.5 ± 0.19122
E30 1.4 ± 1.4703
K10 0.01 ± 0
K20 0.01 ± 0
k30 1E-7 ± 0
alpha 0.1319 ± 0.04999
JMT 2.46593E12 ± 0
Reduced Chi-Sq 0.00444
R-Square (COD 0.99174
Adj. R-Square 0.99125

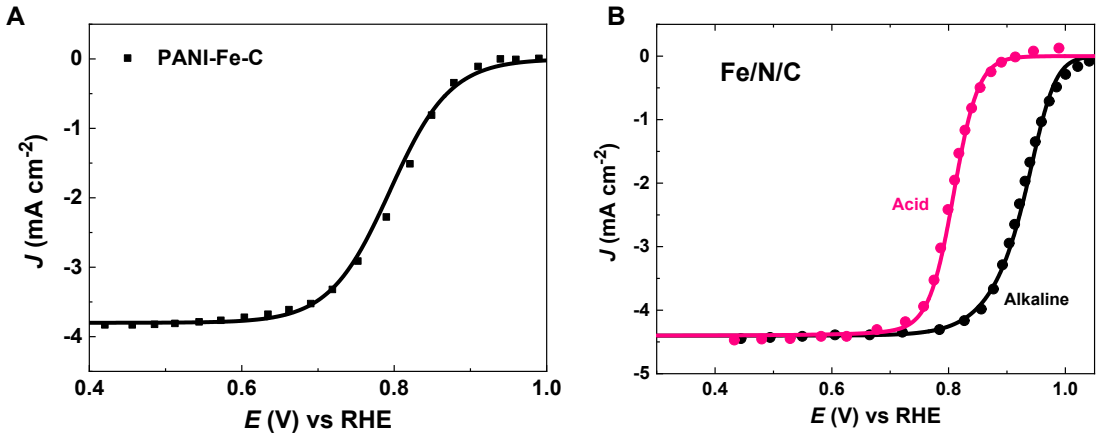

Figure S10. Kinetic modeling of Fe, N doped carbon catalysts in ORR. (*A*) PANI-Fe-C catalyst from ref.[29]. (*B*) AT Fe/N/C catalyst from ref.[30].

Table 3. Fitting results for OER catalysts.

Catalyst	E^0_1 (V)	E^0_2 (V)	E^0_3 (V)	E^0_4 (V)	ΔG_{O*} (eV)
Co_3O_4	1.50	1.56	1.25	0.62	3.06
IrO_2	1.24	1.34	1.46	0.88	2.58
NiFe	1.32	1.42	1.49	0.88	2.74
RuO_2	1.30	1.43	1.38	0.82	2.73
MnO_2	1.16	1.27	1.53	0.96	2.49
TiO_2	1.91	1.83	0.97	0.20	3.75
Fe_2O_3	1.83	1.80	1.00	0.24	3.68
NiOOH	1.32	1.30	1.63	1.22	2.07
CoOOH	1.48	1.54	1.26	0.64	3.02
FeOOH	1.71	1.69	1.12	0.42	3.39
MnOOH	0.76	1.07	1.73	1.36	1.83
CoFe	1.35	1.44	1.50	0.62	2.79
$LaMnO_3$	0.62	0.98	1.82	1.50	1.60
$La_{0.6}Sr_{0.4}MnO_3$	0.74	1.06	1.74	1.38	1.80
$La_{0.2}Ca_{0.8}MnO_3$	0.72	1.05	1.75	1.40	1.77

$LaNiO_3$	1.34	1.45	1.35	0.78	2.79
$LaCoO_3$	1.60	1.62	1.18	0.52	3.22
$La_{0.6}Sr_{0.4}CoO_3$	1.44	1.52	1.28	0.68	2.96
$La_{0.7}Sr_{0.3}FeO_3$	1.70	1.69	1.12	0.42	3.39
$La_{0.5}Sr_{0.5}CoO_3$	1.64	1.65	1.15	0.48	3.29
$LaVO_3$	1.82	1.76	1.04	0.30	3.58
$SrVO_3$	1.86	1.79	1.01	0.26	3.65

Table 4. Fitting results for ORR catalysts.

Catalyst	E^0_1 (V)	E^0_4 (V)	ΔG_{O^*} (eV)
Pt(111)	0.98 ± 0.015	2.14 ± 0.015	2.2 ± 0.022
Pt_3Ni(111)	1.06 ± 0.012	1.06 ± 0.012	2.32 ± 0.017
Pt_3Sc	1.02 ± 0.015	2.10 ± 0.015	2.26 ± 0.030
Pt_3Y	1.05 ± 0.010	2.07 ± 0.010	2.31 ± 0.020
Ag(110)	1.31 ± 0.020	0.81 ± 0.020	2.74 ± 0.023
Fe/N/C	1.18 ± 0.027	0.94 ± 0.027	2.54 ± 0.070
Fe/N/C	1.12 ± 0.027	1.00 ± 0.027	2.40 ± 0.070
PANI-Fe-C	1.19 ± 0.020	0.93 ± 0.020	2.55 ± 0.080
Au	1.18 ± 0.020	0.94 ± 0.020	3.55 ± 0.100
Au/C	1.27 ± 0.020	0.85 ± 0.020	2.69 ± 0.070
N-G	1.18 ± 0.035	0.94 ± 0.035	2.5 ± 0.060
N-G	1.52 ± 0.040	0.6 ± 0.040	3.1 ± 0.120
N-GRW	1.20 ± 0.040	0.92 ± 0.040	2.48 ± 0.085

Note: The modeling results of the catalysts in acid are shown in pink colour, while that in base are shown in black colour.

3.4 The procedure of drawing energy profile based on modeling results

As depicted in Figure 6, there exists a mathematical relationship between extracted potential (E_i^0) with the binding energies of oxygen intermediates. With extracted potential we can directly obtain the binding energies of intermediates before (and include) RDS. With the help of the scaling relationship, we can estimate the binding energies of the remaining intermediates. Therefore, we can depict the reaction energy profile with the energetics of oxygen intermediates. In Figure 3B, we draw our energy diagram based on that the applied potential equals to RHE, thus the total free energy is 4.92 eV for the formation of a O_2 molecule.

$$\Delta G_{\mathrm{OH}^*} = eE_1^0 \quad (27)$$

$$\Delta G_{\mathrm{O}^*} = e(E_1^0 + E_2^0) \quad (28)$$

$$\Delta G_{\mathrm{OOH}^*} = e(E_1^0 + E_2^0 + E_3^0) \quad (29)$$

Where e is the elementary charge in positive value.

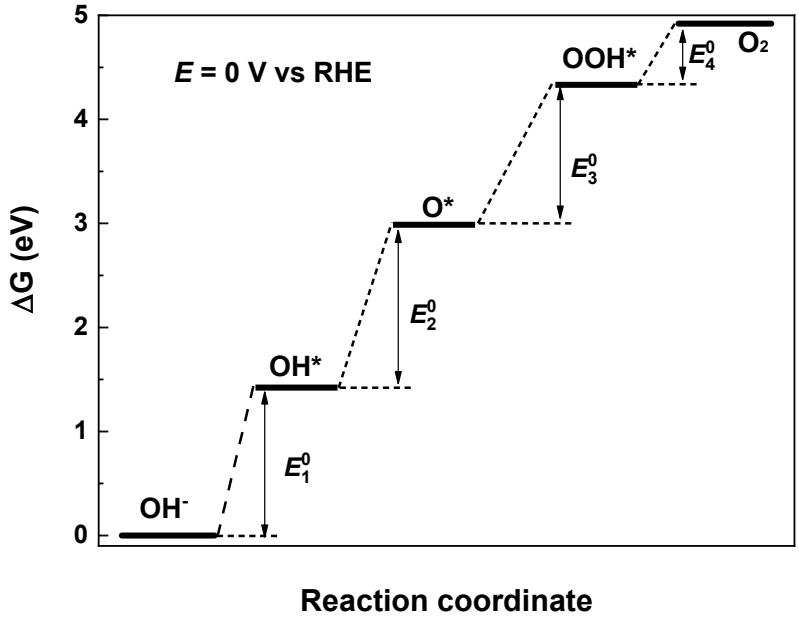

Figure S11. Schematic diagram of the relation between equilibrium potential with potential energy diagram under the applied potential equals to RHE.

Table 5. Comparison between our kinetic model with the model from literature.

	Quantitative interpretation of electrochemical data	**Definition of intermediates adsorption energy**	**Representatives**
Classic kinetic model	✓	×	B.E. Conway, N.M. Markovic
DFT	×	✓	J.K. Norskov
Our model	✓	✓	

Compared with the models summarized above, the major advancement of our model is that we adopt the advantages of the key concepts from the two different approaches to study the energetic origin of intrinsic activity over different catalysts. Therefore, one important application of our kinetic model is to extract intermediate bonding energies through modeling experimental kinetics.

4 Supplementary Figures

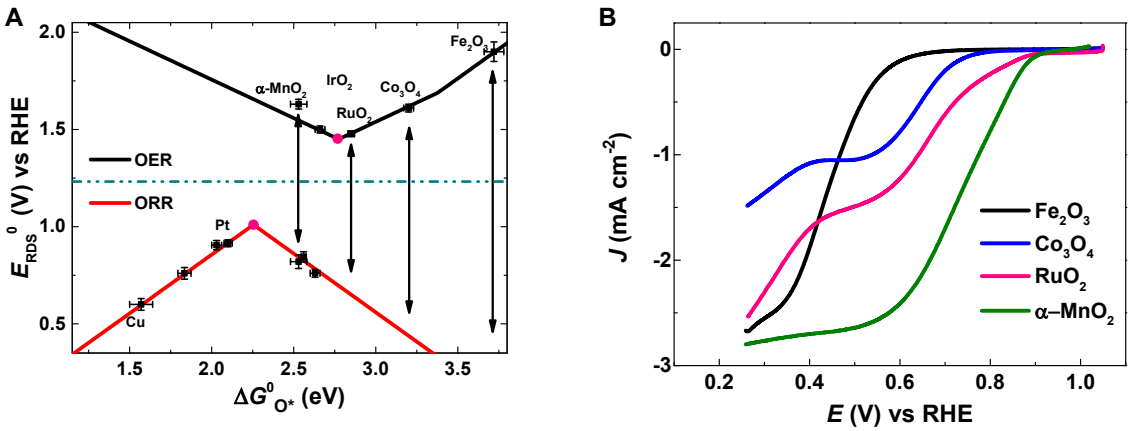

Figure S12. Predicted and experimental ORR activity of common transition metal oxides. (*A*) Predicted ORR activity from OER activity volcano plot. The intersection points for all TMOs are located on the right leg of ORR activity volcano plot, indicating that the RDS of TMOs in ORR should be the activation of O_2. Therefore, the higher the surface reactivity is, the higher catalytic activity in ORR. (*B*) Measured ORR kinetics. The activity increases in the order of $Fe_2O_3 < Co_3O_4 < RuO_2 < \alpha\text{-}MnO_2$, consistent with the predication from our model. The current density for Fe_2O_3 is significantly contributed from glassy carbon electrode as the activity of Fe_2O_3 is very poor.

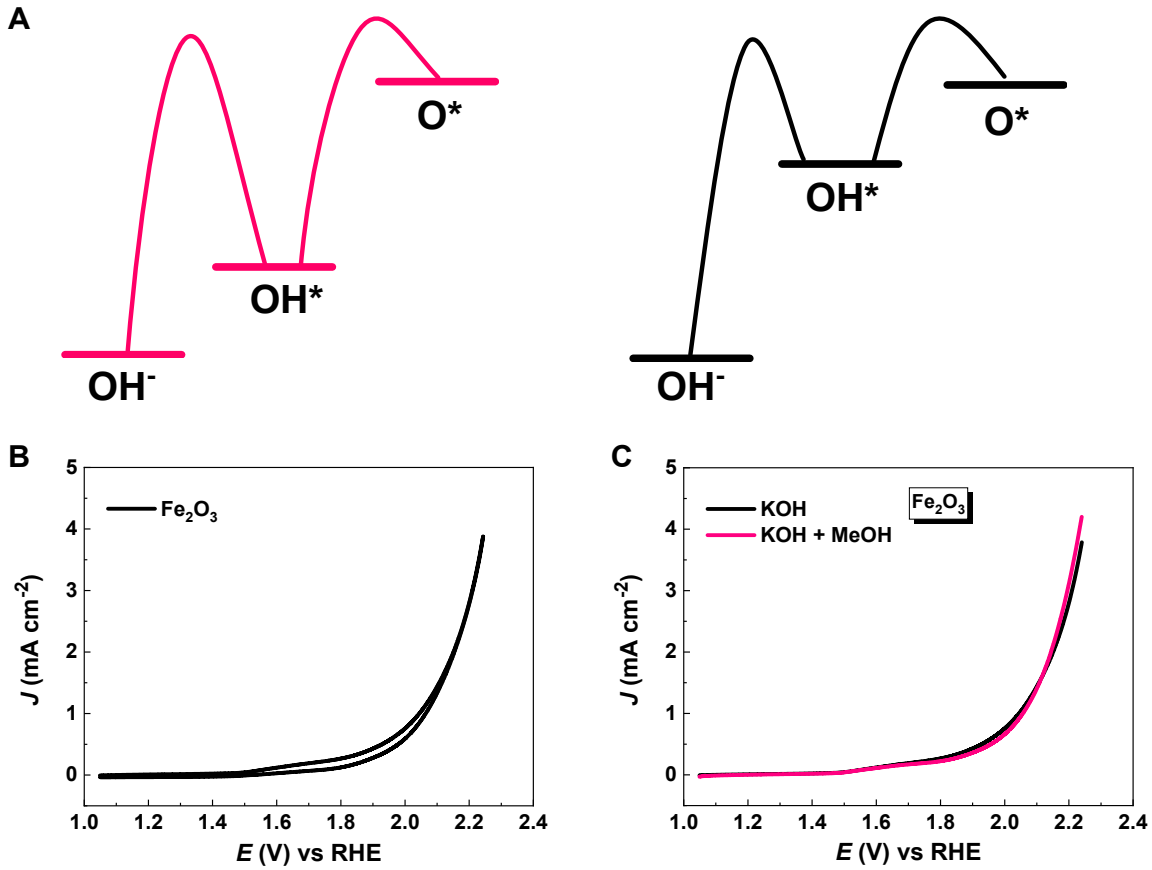

Figure S13. Distinguishing RDS and PDS in OER for first ET step as RDS. (*A*) Schematic energy profile for different binding energy of OH*. If RDS is the same as PDS, the binding of OH* is weak, thus the coverage of OH* would be very low. On the contrary, if second ET step is PDS, the relatively strong binding of OH* would result in significant coverage of OH*. Therefore, one can use this difference to distinguish whether RDS is PDS. (*B*) CV curve of Fe_2O_3 in 1 M KOH. Scan rate: 50 mV/s. No reduction peak can be observed in reverse scan (towards negative potential), suggesting low possibility of OH* adsorption. (*C*) Detecting reactive OH* by methanol (MeOH). Our recent work demonstrates that the OH* generated in OER is electrophile, which can oxidize nucleophiles, such as alcohol molecules. No significant difference in LSV curve can be observed after adding methanol, indicating second ET step is not PDS. The results from CV and methanol detection method are consistent with each other.

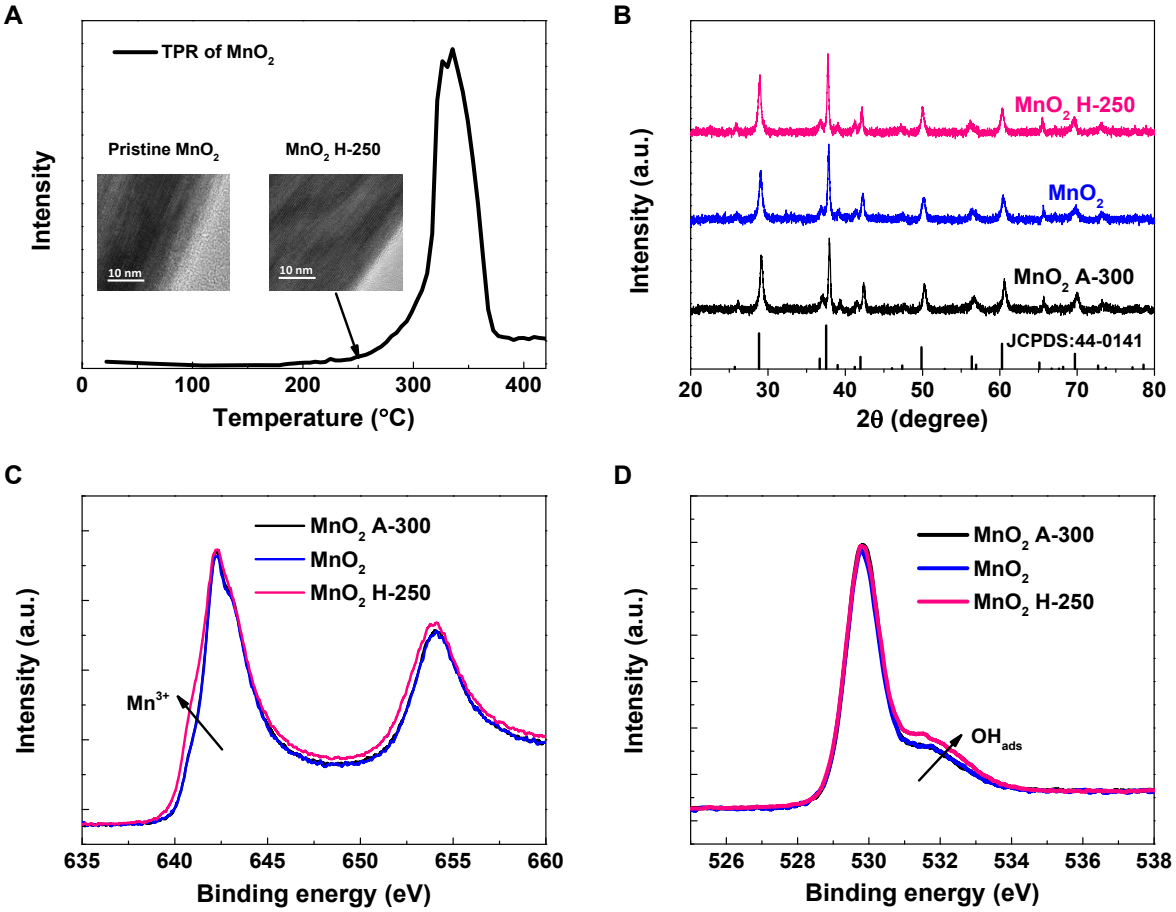

Figure S14. (*A*) TPR spectrum of MnO_2. Insets show the high-resolution transmission electron microscopy (HRTEM) images of original MnO_2 and after calcination at 250 °C in 5% H_2/Ar for 0.5 h, respectively. The bulk and surface structure well remained after treatment. The ramping temperature of both TPR and TPO is 20 °C/min. (*B*) XRD patterns of MnO_2 with varying density of surface Mn_{CUS}. The samples are named with treatment environment and temperature. A and H represent the samples annealed in air and 5% H_2/Ar, respectively, and numbers are the treatment temperature. (*C*) Mn 2p spectra of MnO_2. The increase trend of Mn^{3+} is indicated by the arrow. (*D*) O 1s spectra of MnO_2. Dissociative adsorbed water (OH_{ads}) is shown by the arrow. Surface reactivity of MnO_2 after thermal treatment in reductive atmosphere has been increased.

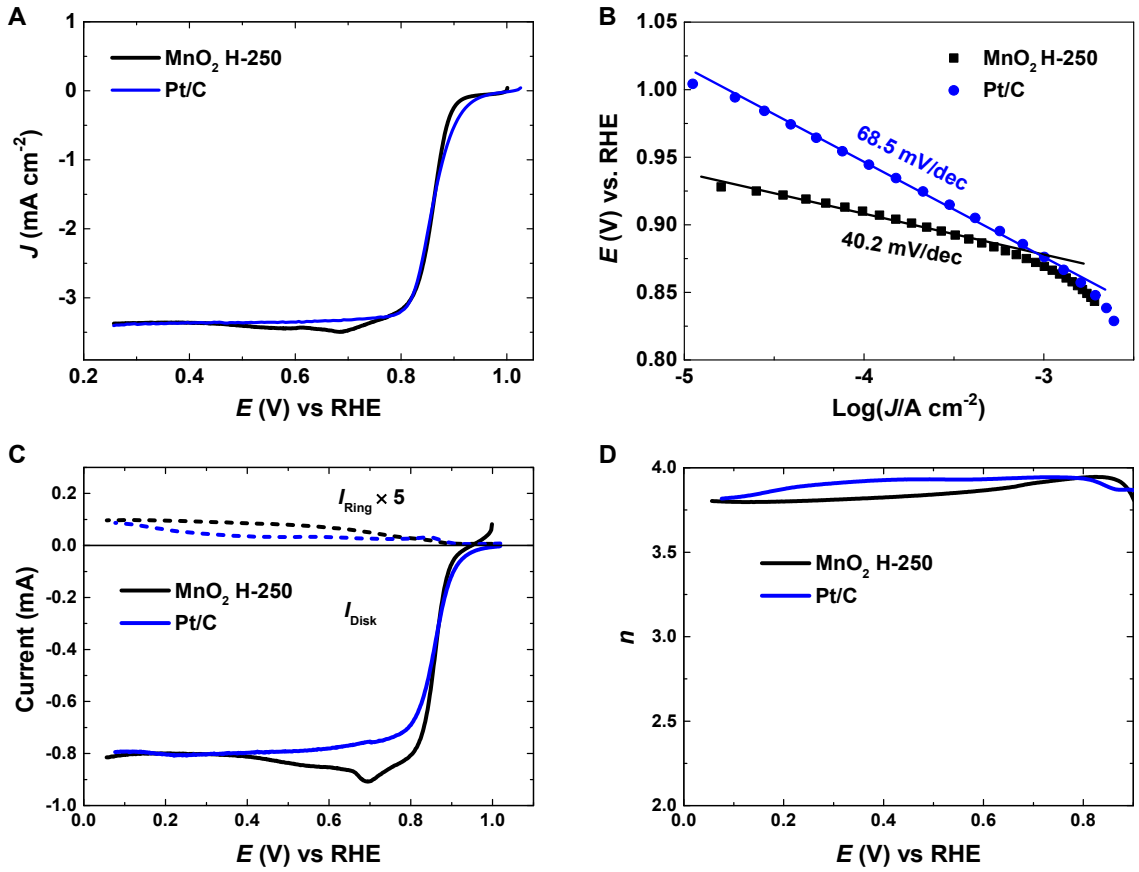

Figure S15. Kinetic comparison between the optimized catalyst with the state-of-the-art catalysts in ORR. (*A*) LSV of optimized MnO_2 and Pt/C in ORR. (*B*) Tafel plots of optimized MnO_2 and Pt/C in ORR. (*C*) RRDE tests of optimized MnO_2 and Pt/C in ORR. (*D*) Calculated electron-transfer number of the optimized MnO_2 and Pt/C in ORR. Scan rate for all LSV and RRDE tests: 5 mV/s.

Besides the apparent kinetics shown in Figure 5 and S12, here we present the kinetic current density normalized to the active surface area in Figure S13, which verifies the intrinsic excellent activity of optimized MnO_2 in ORR.

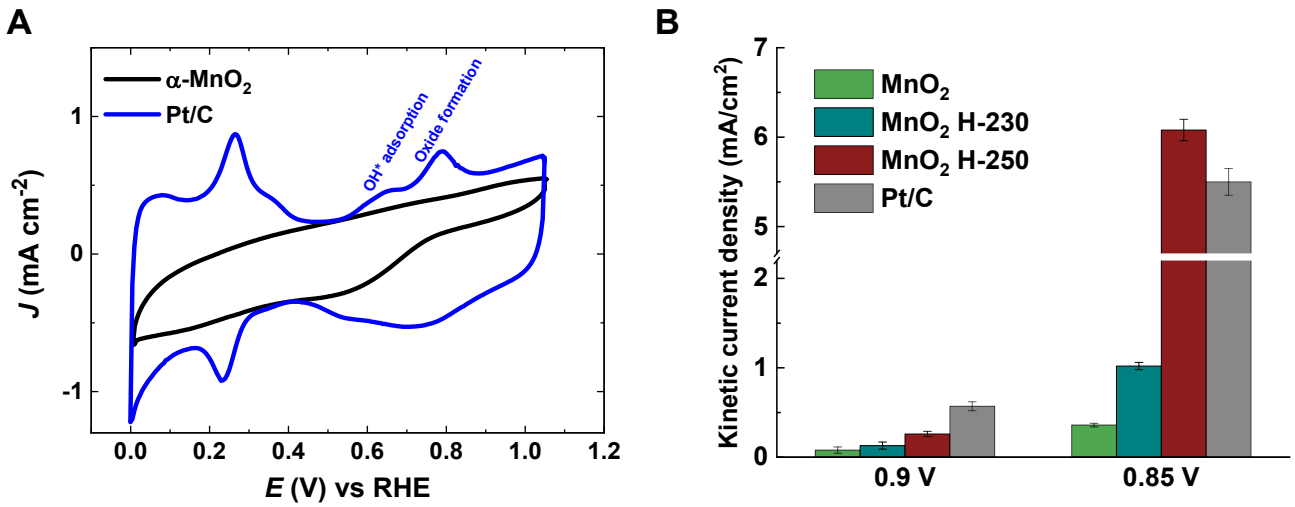

Figure S16. Activity comparison between MnO_2 with Pt/C in ORR. (*A*) Typical CV curves for derive electrochemical active surface area. As MnO_2 is non-precious material, the catalyst loading (500 μg/cm^2) is higher than Pt/C (500 μg/cm^2). However, the specific surface area of MnO_2 is lower than Pt. The calculated ratio of the surface area is 1.2 for MnO_2 to Pt/C. (*B*) Comparison of kinetic current density corrected by surface area.

References

(1) Tao, H. B.; Fang, L.; Chen, J.; Yang, H. B.; Gao, J.; Miao, J.; Chen, S.; Liu, B., Identification of Surface Reactivity Descriptor for Transition Metal Oxides in Oxygen Evolution Reaction. *J. Am. Chem. Soc.* **2016,** *138*, 9978.

(2) Cruz, J.; Baglio, V.; Siracusano, S.; Antonucci, V.; Aricò, A.; Ornelas, R.; Ortiz-Frade, L.; Osorio-Monreal, G.; Durón-Torres, S.; Arriaga, L., Preparation and characterization of RuO2 catalysts for oxygen evolution in a solid polymer electrolyte. *Int J Electrochem Sci* **2011,** *6*, 660.

(3) Subbaraman, R.; Danilovic, N.; Lopes, P. P.; Tripkovic, D.; Strmcnik, D.; Stamenkovic, V. R.; Markovic, N. M., Origin of Anomalous Activities for Electrocatalysts in Alkaline Electrolytes. *J. Phys. Chem. C* **2012,** *116*, 22231.

(4) Chen, R.; Yang, C.; Cai, W.; Wang, H.-Y.; Miao, J.; Zhang, L.; Chen, S.; Liu, B., Use of platinum as the counter electrode to study the activity of nonprecious metal catalysts for the hydrogen evolution reaction. *ACS Energy Lett.* **2017,** *2*, 1070.

(5) Liang, Y.; Li, Y.; Wang, H.; Zhou, J.; Wang, J.; Regier, T.; Dai, H., Co3O4 nanocrystals on graphene as a synergistic catalyst for oxygen reduction reaction. *Nature Mater.* **2011,** *10*, 780.

(6) Zhang, J.; Mo, Y.; Vukmirovic, M. B.; Klie, R.; Sasaki, K.; Adzic, R. R., Platinum Monolayer Electrocatalysts for O2 Reduction: Pt Monolayer on Pd(111) and on Carbon-Supported Pd Nanoparticles. *J. Phys. Chem. B* **2004,** *108*, 10955.

(7) Conway, B.; Jerkiewicz, G., Relation of energies and coverages of underpotential and overpotential deposited H at Pt and other metals to the 'volcano curve'for cathodic H2 evolution kinetics. *Electrochim. Acta* **2000,** *45*, 4075.

(8) Conway, B. E.; Jerkiewicz, G., Nature of electrosorbed H and its relation to metal dependence of catalysis in cathodic H2 evolution. *Solid State Ionics* **2002,** *150*, 93.

(9) Conway, B. E.; Tilak, B. V., Behavior and Characterization of Kinetically Involved Chemisorbed Intermediates in Electrocatalysis of Gas Evolution Reactions. *Adv. Catal.* **1992,** *38*, 1.

(10) Nørskov, J. K.; Rossmeisl, J.; Logadottir, A.; Lindqvist, L.; Kitchin, J. R.; Bligaard, T.; Jónsson, H., Origin of the Overpotential for Oxygen Reduction at a Fuel-Cell Cathode. *J. Phys. Chem. B* **2004,** *108*, 17886.

(11) Koper, M. T. M., Thermodynamic theory of multi-electron transfer reactions: Implications for electrocatalysis. *J. Electroanal. Chem.* **2011,** *660*, 254.

(12) Bard, A. J.; Faulkner, L. R., *Electrochemical methods: fundamentals and applications*. John Wiley & Sons, Inc: 2001.

(13) Doyle, R. L.; Lyons, M. E. G., The Oxygen Evolution Reaction: Mechanistic Concepts and Catalyst Design. In *Photoelectrochemical Solar Fuel Production: From Basic Principles to Advanced Devices*, Giménez, S.; Bisquert, J., Eds. Springer International Publishing: Cham, 2016; pp 54.

(14) De Faria, L. A.; Boodts, J. F. C.; Trasatti, S., Electrocatalytic properties of ternary oxide mixtures of composition Ru0.3Ti(0.7−x)CexO2: oxygen evolution from acidic solution. *J. Appl. Electrochem.* **1996,** *26*, 1195.

(15) Surendranath, Y.; Nocera, D. G., Oxygen Evolution Reaction Chemistry of Oxide-Based Electrodes. In *Prog. Inorg. Chem.*, D., K. K., Ed. John Wiley & Sons, Inc.: 2011; Vol. 57, pp 537.

(16) Davis, R. E.; Horvath, G. L.; Tobias, C. W., The solubility and diffusion coefficient of oxygen in potassium hydroxide solutions. *Electrochim. Acta* **1967,** *12*, 287.

(17) Garcia, A. C.; Koper, M. T. M., Effect of Saturating the Electrolyte with Oxygen on the Activity for the Oxygen Evolution Reaction. *ACS Catal.* **2018,** *8*, 9359.

(18) Stamenkovic, V.; Markovic, N., Oxygen reduction on platinum bimetallic alloy catalysts. *Handbook of Fuel cells* **2009**.

(19) Stamenkovic, V. R.; Fowler, B.; Mun, B. S.; Wang, G.; Ross, P. N.; Lucas, C. A.; Marković, N. M., Improved Oxygen Reduction Activity on Pt3Ni(111) via Increased Surface Site Availability. *Science* **2007,** *315*, 493.

(20) Holewinski, A.; Linic, S., Elementary Mechanisms in Electrocatalysis: Revisiting the ORR Tafel Slope. *J. Electrochem. Soc.* **2012,** *159*, H864.

(21) Shao, M. H.; Adzic, R. R., Spectroscopic Identification of the Reaction Intermediates in Oxygen Reduction on Gold in Alkaline Solutions. *J. Phys. Chem. B* **2005,** *109*, 16563.

(22) Quaino, P.; Luque, N.; Nazmutdinov, R.; Santos, E.; Schmickler, W., Why is gold such a good catalyst for oxygen reduction in alkaline media? *Angew. Chem. Int. Ed.* **2012,** *51*, 12997.

(23) Rodriguez, P.; Kwon, Y.; Koper, M. T., The promoting effect of adsorbed carbon monoxide on the oxidation of alcohols on a gold catalyst. *Nature Chem.* **2011,** *4*, 177.

(24) Walter, M. G.; Warren, E. L.; McKone, J. R.; Boettcher, S. W.; Mi, Q.; Santori, E. A.; Lewis, N. S., Solar water splitting cells. *Chem. Rev.* **2010,** *110*, 6446.

(25) Hansen, H. A.; Viswanathan, V.; Nørskov, J. K., Unifying Kinetic and Thermodynamic Analysis of 2 e– and 4 e– Reduction of Oxygen on Metal Surfaces. *J. Phys. Chem. C* **2014,** *118*, 6706.

(26) Greeley J.; Stephens, I. E. L.; Bondarenko, A. S.; Johansson, T. P.; Hansen, H. A.; Jaramillo, T. F.; Rossmeisl J.; Chorkendorff I.; Nørskov, J. K., Alloys of platinum and early transition metals as oxygen reduction electrocatalysts. *Nature Chem.* **2009,** *1*, 552.

(27) Nørskov, J. K.; Bligaard, T.; Logadottir, A.; Kitchin, J.; Chen, J. G.; Pandelov, S.; Stimming, U., Trends in the exchange current for hydrogen evolution. *J. Electrochem. Soc.* **2005,** *152*, J23.

(28) Gorlin, M.; Chernev, P.; Ferreira de Araujo, J.; Reier, T.; Dresp, S.; Paul, B.; Krahnert, R.; Dau, H.; Strasser, P., Oxygen Evolution Reaction Dynamics, Faradaic Charge Efficiency, and the Active Metal Redox States of Ni-Fe Oxide Water Splitting Electrocatalysts. *J. Am. Chem. Soc.* **2016,** *138*, 5603.

(29) Wu, G.; More, K. L.; Johnston, C. M.; Zelenay, P., High-performance electrocatalysts for oxygen reduction derived from polyaniline, iron, and cobalt. *Science* **2011,** *332*, 443.

(30) Rauf, M.; Zhao, Y.-D.; Wang, Y.-C.; Zheng, Y.-P.; Chen, C.; Yang, X.-D.; Zhou, Z.-Y.; Sun, S.-G., Insight into the different ORR catalytic activity of Fe/N/C between acidic and alkaline media: Protonation of pyridinic nitrogen. *Electrochem. Commun.* **2016,** *73*, 71.